Published in final edited form as:
IEEE J Sel Top Signal Process. 2013 February ; 7(1): . doi:10.1109/JSTSP.2012.2237380.

Anomaly Detection and Artifact Recovery in PET Attenuation-Correction Images Using the Likelihood Function

Charles M. Laymon and
Department of Radiology, University of Pittsburgh, Pittsburgh, PA, 15213 USA

James E. Bowsher
Department of Radiation Oncology, Duke University, Durham, NC 27710, USA

Charles M. Laymon: CML14@pitt.edu; James E. Bowsher: James.Bowsher@duke.edu

Abstract

In dual modality PET/CT, CT data are used to generate the attenuation correction applied in the reconstruction of the PET emission image. This requires converting the CT image into a 511-keV attenuation map. Algorithms for making this transformation require assumptions about the makeup of material within the patient. Anomalous material such as contrast agent administered to enhance the CT scan confounds conversion algorithms and has been observed to result in inaccuracies, *i.e.*, inconsistencies with the true 511-keV attenuation present at the time of the PET emission scan. These attenuation artifacts carry through to the final attenuation-corrected PET emission image and can resemble diseased tissue. We propose an approach to correcting this problem that employs the attenuation information carried by the PET emission data. A likelihood-based algorithm for identifying and correcting of contrast is presented and tested. The algorithm exploits the fact that contrast artifacts manifest as too-high attenuation values in an otherwise high quality attenuation image. In a separate study, the performance of the loglikelihood as an objective-function component of a detection/correction algorithm, independent of any particular algorithm was mapped out for several imaging scenarios as a function of statistical noise. Both the full algorithm and the loglikelihood performed well in studies with simulated data. Additional studies including those with patient data are required to fully understand their capabilities.

I. Introduction

Positron Emission Tomography (PET) is a nuclear medicine imaging modality in which a positron-emitting radio tracer is administered to the patient. The most commonly used PET radiotracer is ^{18}F-labeled fluorodeoxyglucose (FDG), a glucose analog that accumulates in metabolically active cells and is particularly useful for oncology studies. Emitted positrons annihilate with ambient electrons producing two 511-keV photons emitted with an opening angle of 180°. The PET scanner consists of a cylindrical array (typically 15–30 cm axial extent with a diameter of about 80 cm for human scanners) of small detectors (typically a few mm^2 surface area) arranged around the subject. The scanner identifies annihilation events by the near simultaneous observation of two 511 keV photons in different detectors (coincidence event). The two triggered detectors determine the line [line-of-response (LOR)] along which the event took place. The count rates so determined along the various detector-defined LORs passing through the patient provide the data sufficient for reconstructing an image of tracer concentration. The set of LOR count rate data is commonly referred to as a sinogram.

However the attenuation of the emitted 511 keV photons by the patient must be accounted for. Attenuation is characterized in terms of an attenuation coefficient, μ, that is a function of the photon energy and the attenuating material. The probability $P(\vec{r_i}, \vec{r_f})$ of a photon

surviving transit along a path from point $\vec{r_i}$ (its creation point) to $\vec{r_f}$ (its detection point) through matter characterized by attenuation coefficient $\mu(\vec{r})$ is given by

$$P(\vec{r_i}, \vec{r_f}) = \exp\left[-\int_{\vec{r_i}}^{\vec{r_f}} \mu(\vec{r}) ds\right] \quad (1)$$

where the integral is taken along the line connecting the integration limits. To set the scale, the attenuation coefficient for 511-keV photons in liquid water is approximately $\mu = 0.096$ cm^{-1}[1]. The probability (or attenuation factor) for a *coincidence event* to survive attenuation is the product of the probabilities that the individual photons survive and is given by equation (1) but with the integral taken along an entire LOR connecting two detectors. Attenuation factors for each LOR can thus be calculated from a spatial map (i.e. image) of 511 keV μ-values using equation (1) along each LOR. Production of attenuation factors is an integral part of each scan since they are required to correct the observed count rates along each LOR.

Typically 511 keV μ maps are obtained from a CT scan acquired as part of a PET/CT [2] session and algorithms have been developed [3] [4] [5] [6] for transforming CT-units to 511 keV μ-values. However, any such transformation is ambiguous since attenuation is dependent on atomic number (Z), atomic density, and energy. In practice, transformations have been implemented by assuming that the body consists of constrained mixtures of some basic tissue types, *e.g.,* soft tissue, bone, and water [7] [8] [3] [4] [5]. Any anomalous material results in an inaccuracy in the 511 keV μ-value deduced from the CT data and ultimately in the PET image. CT contrast agent such as organically bound iodine (Z=53) is a particularly vexing anomaly. It is administered intravenously or orally to enhance the circulatory system and digestive tract and has a Z-value far above that of calcium (Z=20) and thus has the potential for producing large μ-value errors and related PET inaccuracies. This problem can, in principle, be avoided by not performing CT scans for attenuation correction with contrast on board the patient. However, most clinical CT scans are performed with contrast so that this avoidance method would require a separate CT scan for attenuation correction along with a corresponding increased radiation dose to the patient. Thus contrast enhanced CT scans are frequently used for attenuation correction.

Antoch et al. [9] have pointed out that, in some cases, the resultant artifacts in attenuation-corrected emission images can resemble diseased tissue. Figure 1 is an example from a clinical FDG PET/CT scan with intravenous (IV) contrast. Parts (a) and (b) of the figure show coronal and transaxial views of the attenuation-corrected PET image. The arrows indicate a region of apparent increased tracer uptake. This hot spot has been interpreted as being an artifact of the attenuation correction and not due to increased FDG uptake. This conclusion was reached by examination of the same area of the CT (c), which shows a region of contrast enhancement, and the uncorrected PET image (d), which does not indicate increased FDG uptake.

The objective of the present work is to develop methods to identify and reduce artifacts in the attenuation correction for PET by using the information content of emission data.

There has been much previous work on estimating attenuation from emission projection data, e.g., [10] [11] [12] [13] [14] [15] [16] [17] [18] [19] [20] [21] [22] [23] [24]. However, the task undertaken here differs from the tasks pursued in previous studies in a major way. The goal of previous work was mainly to reconstruct an attenuation image or to jointly reconstruct attenuation and emission images without the benefit of transmission/attenuation data. Here, we use the fact that, in the PET/CT modality, a high-quality, low-noise

attenuation image is always available. However, an attenuation image may have anomalies resulting from spurious CT-to-511-keV conversion in regions with contrast. Therefore the current task is the detection and correction of these anomalies.

Determination of a full PET attenuation map without transmission data is problematic e.g. [19] [23], A more feasible task may be that proposed here: the detection of anomalies in an *existing* attenuation map, wherein the regions that might contain anomalies are limited in volume and can be identified by simple methods such as thresholding. We hypothesize that PET emission data contain sufficient information to be of practical value in detecting and correcting such anomalies.

The remainder of this paper is organized as follows. In Section II-A a loglikelihood is presented that is a function of emission parameters and a *limited* number of attenuation parameters. In Section II-B the loglikelihood is utilized as the basis for an algorithm to recover correct attenuation values in anomalous regions while leaving other voxels largely unchanged. The algorithm also provides for detection, which can be accomplished by comparing attenuation images before and after algorithm use, e.g. by a threshold on voxel changes. Section III describes evaluation methods, which include evaluation of the recovery algorithm and an ROC study assessing detectability based on algorithm results, Section III also describes methods for assessing directly, independent of any specific algorithm, the ability of the loglikelihood to distinguish artifactual from non-artifactual structures for several discrimination tasks relevant to anomaly detection. Results of these various evaluations are given in Section IV. A discussion of the significance and limitations of this work presented in Section V, with conclusions in Section VI.

II. Objective Function and Detection/Correction Algorithm

A. A Model for Attenuation Artifact Recovery

A general framework for statistical, iterative image reconstruction is to generate images that increase an objective function:

$$\Phi = L - \beta P \quad (2)$$

where L is a loglikelihood function. The penalty function, P, specifies constraints on the image values, and β determines the relative influence of L and P. To within a constant, the emission Poisson loglikelihood function is

$$L = -\sum_i (M_i - Y_i \ln M_i) \quad (3)$$

where Y_i is the measured number of events along line of response (LOR) i. For PET, the expected number of events can be expressed as

$$M_i = b_i + \sum_j c_{ij} \lambda_j \exp(-\sum_k \mu_k l_{ik}). \quad (4)$$

In equation (4) λ_j is the expected number of positron emissions in pixel j, and c_{ij} is the probability that a positron emitted within pixel j will result in an event along LOR i, assuming no accidental coincidences, no scatter, and no attenuation. The term b_i is the expected number of accidental-coincidence and scatter events along LOR i. The symbol l_{ik} denotes the path length of LOR i through pixel k and μ_k is the linear attenuation coefficient for pixel k. The expression $\exp(-\Sigma_k \mu_k l_{ik})$ is the probability that the two 511-keV photons

will both survive attenuation as they traverse LOR i en route to the PET detectors. When μ is known, e.g. from a transmission scan, equation (4) may be written as

$$M_i = b_i + \sum_j p_{ij} \lambda_j, \quad (5)$$

where $p_{ij} = c_{ij} \exp(-\Sigma_k \mu_k l_{ik})$. Equations (3) and (5) express the familiar loglikelihood function appropriate for PET. Many algorithms, e.g. [25] [26] [27] [28] [29], have been developed for generating iterates of λ that successively increase Φ – with L given by equations (3) and (5) and with the attenuation μ fixed – thereby providing a method for PET image reconstruction.

Equations (2)–(4) can also be considered as functions of μ. Since the summation within the exponential of equation (4) is independent of the pixel j along which positron emission occurs, equation (4) can be written as

$$M_i = b_i + S_i \exp(-\sum_k \mu_k l_{ik}) \quad (6)$$

where $S_i = \Sigma_j c_{ij} \lambda_j$. Equation (6) indicates that for purposes of estimating attenuation from PET projections, the activity distributed along LOR i is equivalent to a point source located external to the patient and along LOR i. When S_i is known, equations (3) and (6) specify the Poisson loglikelihood for transmission image reconstruction. Algorithms, for example [27] [26] [30] [31], have been developed for generating iterates of μ that successively increase Φ with L given by equations (3) and (6) and with the activity S fixed, thereby providing transmission image reconstruction. Estimation of full activity and attenuation images from emission data can be accomplished by interleaving updates of activity, λ, based on equations (2), (3), (5) (with attenuation μ fixed) and updates of μ based on equations (2), (3), and (6) (with λ fixed), as in [19] [23]. These updates can be accomplished by any of the algorithms that have been developed for emission and transmission image reconstruction based on equations (5) and (6) respectively.

The purpose of the current work is to estimate the full radiotracer activity distribution and simultaneously to estimate *limited portions* of the attenuation image, where the remainder of the attenuation image is established by CT-to-511-keV mapping. In terms of the above discussion, we consider the expected sinogram values

$$\begin{aligned} M_i &= b_i + \sum_j c_{ij} \lambda_j \exp(-\sum_{k \in \mathcal{F}} \mu_k l_{ik}) \exp(-\sum_{k \in \mathcal{D}} \mu_k l_{ik}) \\ &= b_i + A_i' \sum_j c_{ij} \lambda_j \exp(-\sum_{k \in \mathcal{D}} \mu_k l_{ik}) \end{aligned} \quad (7)$$

where $A_i' = \exp(-\sum_{k \in \mathcal{F}} \mu_k l_{ik})$ is a constant, $\mathcal{F}$ specifies the set of pixels in which attenuation is fixed to the values obtained by CT, and $\mathcal{D}$ specifies the set of pixels that have been identified as *potentially* including attenuation artifacts. Herein the partition $\mathcal{D}$ is referred to as the ”dynamic region” and $\mathcal{F}$ as the ”static region”. The partitioning of the attenuation images into $\mathcal{D}$ and $\mathcal{F}$ can be adjusted by the user on a case-by-case basis. Possible criteria for selecting $\mathcal{D}$ include suspicious regions and regions with attenuation above that of soft tissue. This is an appropriate choice for the commonly occurring situation in which the CT-to-PET scaling algorithm improperly assigns too-high μ-values to regions containing contrast agent.

If equation (7) is considered as a function of activity λ, with μ fixed, then it reduces to the form of equation (5). If, however, equation (7) is considered as a function of $\{\mu_k: k \in \mathcal{D}\}$, with λ fixed, then it reduces to

$$M_i = b_i + S_i' \exp(-\sum_{k \in \mathcal{D}} \mu_k l_{ik}) \quad (8)$$

where $S_i' = (\sum_j c_{ij} \lambda_j) \exp(-\sum_{k \in \mathcal{F}} \mu_k l_{ik})$. Equation (8) is formally equivalent to equation (6). Thus, as in earlier work on estimating activity and full attenuation images from emission data, interleaved updates of activity (λ) using equation (5) and of $\{\mu_k: k \in \mathcal{D}\}$ using equation (8) can be used to estimate an activity image and *limited portions* of the corresponding attenuation map.

Although formally equivalent, equations (6) and (8) are substantially different operationally. Whereas all μ-values in the image constitute the unknowns of equation (6), only a small subset of pixels contribute to the unknowns of equation (8), with the majority of the attenuation parameters in equation (8) being fixed by the transformed CT image. Furthermore, the few unknowns in equation (8) may be clustered together into only a few artifacts with the concurrent expectation of similar attenuation values within each artifact, so that standard Gibbs distribution smoothing penalties are reasonable as additional constraints on the attenuation image. Hence, estimation may be considerably better conditioned with equation (8) than with equation (6). In this work, we investigate the utility of PET emission data for correcting artifacts of limited spatial extent in CT-based 511-keV attenuation images.

B. Detection/Correction Algorithm

1) Dynamic Region—Image pixels are divided into two classes. The dynamic class ($\mathcal{D}$) consists of all pixels with attenuation values that are allowed to be changed by the algorithm. The static set ($\mathcal{F}$) contains the remaining pixels which are fixed to their CT-derived values.

Any set of pixels could be chosen as the dynamic region, including, in principle, the entire image. However, choosing an overly large region can only hurt performance. Since anomalous material such as contrast produces too-high μ-values, an appropriate choice is to assign pixels with attenuation values above those of soft-tissue to the dynamic region. With this choice, the dynamic region would consist mainly of bone with occasional contrast artifacts.

2) Algorithm Operation—Joint image reconstruction of the radiotracer distribution $\{\lambda_j\}$ and dynamic region $\mathcal{D}$ of the attenuation distribution is enabled by the objective-function form Φ of equation (2) and the loglikelihood L given by equations (3) and (7). Attenuation parameters $\{\mu_k: k \in \mathcal{F}\}$ are fixed at their CT-derived values. Attenuation parameters $\{\mu_k: k \in \mathcal{D}\}$ are allowed to take on the continuum of nonnegative values, as are all activity parameters $\{\lambda_j: j \in \mathcal{D} \cup \mathcal{F}\}$ throughout the image.

For the penalty function component, P of equation (2), the Generalized Gaussian Markov Random Field (GGMRF) model [32] is applied to attenuation values only and is given by

$$P=\frac{1}{2}\sum_{j,k} b_{jk}|\mu_j-\mu_k|^q. \quad (9)$$

The values of the b_{jk} determine the weighting of the various pixel pairs and were set to 1 for the 8 nearest neighbors in 2D, and to zero otherwise. The exponent parameter q can be adjusted in the range from $1 < q \leq 2$. Here, a value of 1.001 was used, yielding an approximate absolute value potential function [32]. The strength of the penalty was determined by processing a set of images using a range of values for β and making a qualitative judgment. Neither q nor the strength parameter β were rigorously optimized. A similar penalty could be, but was not applied based on the emission image.

The objective function Φ is increased, with respect to $\{\lambda_j: j \in \mathcal{D} \cup \mathcal{F}\}$ and $\{\mu_k: k \in \mathcal{D}\}$, by interleaving two procedures, designated below as type 1 and type 2. This algorithm, illustrated in figure 2 yields a reconstructed activity image and a recovered attenuation image.

In the type-1 procedure, attenuation and activity values $\{\lambda_j, \mu_j: j \in \mathcal{D}\}$ within the dynamic region $\mathcal{D}$ are updated using the Iterative Coordinate Descent (ICD) algorithm [33]. During an update, each pixel in the dynamic region is visited once on a random schedule. The pixel's attenuation value is updated first, followed by its emission value. This process increases the objective function Φ at each step.

In the type-2 procedure, all attenuation parameters are fixed at their current values, and *all* activity parameters $\{\lambda_j: j \in \mathcal{D} \cup \mathcal{F}\}$ are updated by OSEM [34]. Here, each type-2 procedure used 1 iteration of OSEM with 9 subsets. Each iteration of the detection/correction algorithm involves one type-1 and one type-2 procedure.

III. Evaluation Methods

A. Production of Simulated Data

Simulation studies were conducted using a digital anthropomorphic (Zubal) phantom [35] consisting of a volumetric CT-based human image in which the various tissue types have been delineated and assigned an index number. A true attenuation phantom was produced by assigning 511-keV attenuation-coefficient values to the Zubal phantom. The tissue-type-to-attenuation-coefficient mapping for this purpose was taken from the emission tomography simulation software package SimSET [36]. Otherwise, SimSET was not used in this work. Similarly, the emission phantom was formed by assigning activity concentrations to each tissue type. Various artifactual attenuation images were produced by modifying the true attenuation phantom. All digital phantoms in this study had a pixel width of 0.4 cm with each slice represented as a 128x128 pixel array.

Sets of similar studies were done using transaxial slices at the chest level and shoulder level. Figure 3 illustrates the true attenuation and emission phantom slices used in this work. Each pair of true attenuation and emission phantoms was forward projected to generate a true attenuated, noise-free emission sinogram, one for the shoulder and one for the chest. Noisy (or "measured") emission sinograms were produced by a Poisson randomization of the noise-free sinogram. For both pairs of attenuation and emission phantoms, 128 measured emission sinogram noise realizations (variates) were produced for each of 7 statistical noise levels corresponding to mean total sinogram counts of 10^3, 10^4, 5×10^4, 10^5, 5×10^5, 10^6, and 10^7. Count levels in this simulation study, which neglects the effects of corrections for random coincidences, scatter, as well as PET resolution effects, cannot be equated directly

with clinical data but should be interpreted in a relative sense. Fig. 4 serves to set the scale and shows example reconstructions at several simulation count levels.

B. Detection/Correction Algorithm Evaluation

The detection/correction algorithm was tested using the simulated chest-level data corresponding to 100000 simulated sinogram counts, generated as described in section III-A. The artifactual attenuation map, illustrated in figure 5, included a 26-pixel artifact of bone-like values in place of soft tissue. The dynamic class $\mathcal{D}$ was taken to be all pixels with attenuation values above that of soft tissue. This included the 26-pixel artifact (region R1) plus the remaining 603 pixels of correctly assigned bone values (i.e. true bone; region R2). Note that in this test, the dynamic class of pixels, $\mathcal{D}$, consists of all pixels in R1 or R2, and the static class, $\mathcal{F}$, consists of all other pixels. Perfect algorithm would restore the μ-values of the R1 pixels to their correct soft-tissue values while leaving all the R2 pixels unchanged.

Each of the 128 noise-variates belonging to the 100000-count sinogram ensemble were processed by 9 iterations of the detection/correction algorithm, generating 128 9-iteration sequences of reconstructed emission images and recovered attenuation maps.

Several figures of merit (FOMs) were defined to quantify error in attenuation images:

$$ME_R = \frac{1}{\mu_R}\frac{\sum_{i\in R}\sum_j(\mu_{ij}-\mu_R)}{n_R N_V}$$
$$RMSE_R = \frac{1}{\mu_R}\sqrt{\frac{\sum_j\left[\frac{\sum_{i\in R}(\mu_{ij}-\mu_R)}{n_R}\right]^2}{N_V}} \quad (10)$$
$$RMSE_{Rp} = \frac{1}{\mu_R}\sqrt{\frac{\sum_j\sum_{i\in R}(\mu_{ij}-\mu_R)^2}{n_R N_V}}$$

where μ_{ij} is the estimated attenuation coefficient of pixel i in variate j and μ_R is the correct value of μ within region R. The symbol n_R represents the number of pixels in region R and $N_V = 128$ is the total number of variate images.

The quantity ME_R is the fractional mean error of all pixels in region R over all variates and is therefore a measure of bias; $RMSE_R$ is the RMS error in region R on regional basis taken over all variates; and $RMSE_{Rp}$ is the RMS error in region R on a pixel basis taken over all pixels and variates. Each of these errors is expressed as a fraction of the true μ-value of the region. For perfect attenuation images, each FOM is zero. In the initial artifactual images, each FOM is equal to zero in the region of true bone (R2) but will have elevated values in R1. The final images resulting from a perfect algorithm would yield zero for all FOMs in both regions.

The FOM values were calculated for both the 26-pixel artifact region ($R = R1$) and the 603-pixel true-bone region ($R = R2$) of the final (iteration-9) recovered attenuation image. For comparison, these values were also calculated for the starting, artifactual attenuation image.

The algorithm, as presented, results in a corrected image. However, it could be used specifically for the task of detection of anomalous image content. At the conclusion of the algorithm all pixels in the dynamic region have a particular μ-value that may be different from the initial value. Ideally, the algorithm should lower the μ values of pixels with initial contrast artifacts (R1 region) while leaving true bone pixels (R2) unchanged. A simple method for implementing the detection task is to apply a μ threshold to the dynamic region of the final attenuation image in which it is assumed that pixels with final values below the

threshold correspond to anomalous material (i.e. IV contrast). A receiver operating characteristic (ROC) study was conducted to evaluate the algorithm for the detection task. The study was performed on pixel-wise basis. The rate of correct or incorrect classification of pixels in the R1 and R2 regions over all 128 images was determined as a function of a μ-threshold value. The area under the curve (AUC) of P_{tp} versus P_{fp} was calculated where P_{tp} is the probability that a pixel belonging to region R1 is correctly classified (i.e., true positive rate) and P_{fp} is the probability that a pixel belonging to R2 is incorrectly classified as belonging to region R1 (i.e., false positive rate).

C. Likelihood Information Content Evaluation

In this section, the general performance of the loglikelihood, *independent of any specific algorithm*, for several discrimination tasks relevant to artifact identification is examined as a function of noise. In each of several studies, 128 noisy emission sinograms were generated at each of 7 noise levels, as described in section III-A. From each measured emission sinogram, two activity images were reconstructed, one using a less-artifactual attenuation image and one using a more-artifactual attenuation image. For each reconstruction, the loglikelihood L was calculated using equations (3) and (7). Each pair of reconstructed images was classified as a winner or loser based on whether L was higher for the reconstruction using the less artifactual attenuation. An accuracy for each imaging scenario and each simulated sinogram count level was calculated by dividing the winner tally by the total number of noise variates (in this case, 128). For these studies, reconstruction of emission data was performed by OSEM [34] using 4 iterations of 9 subsets. Subsections III-C1 to III-C4 below describe the different attenuation artifacts considered. In all, over 10,000 images were reconstructed and evaluated.

1) Bone-like Inconsistencies in Soft Tissue—Small artifacts with attenuation values equal to bone were inserted in place of soft tissue to form artifactual attenuation images.

- **a.** 13-Pixel Single Region: A single 13-pixel bone-valued artifact was included in the artifactual attenuation image. Figure 4 shows the artifactual attenuation image for both the shoulder and chest. Also shown in the figure are sample emission reconstructions using the artifactual attenuation sinograms with varying noise levels.
- **b.** Two Adjacent Regions: A study similar to that outlined in the preceding paragraph was conducted. In this case a second 13-pixel bone-valued artifact was included adjacent to the original artifact. Figure 5 shows the attenuation images with artifacts. The set of measured emission sinograms used was identical to that for the *Single Region* studies. Adding a second artifactual region and analyzing the one- and two-artifact results together provided a study of the ability of L to discriminate attenuation images with fewer artifacts from images with more artifacts.

2) Soft-Tissue-Like Inconsistencies in Bone—Section III-C1 concerns the ability of L to discern bone-like artifacts in soft tissue. For completeness, we also map the performance of L for identifying soft-tissue like inconsistencies in bone. Such artifacts are *not* expected from anomalous contrast in CT-based PET attenuation images. However, this information could be useful in the development of detection or correction algorithms. For example, an iterative algorithm could, during some point in its operation, step into a situation in which it needs to be able to identify attenuation values that are too low. To address this, artifactual attenuation images were formed by replacing 13-pixel regions in bone with soft-tissue values as illustrated in figure 6.

3) Intermediate-Valued Artifacts in Soft Tissue—To test the ability of L to identify artifacts in soft tissue that have values less than that of bone, the study of section III-C1(a) was repeated with the attenuation-coefficient value of the 13-pixel artifact set to a value intermediate between bone and soft tissue.

4) Single Pixel—For a severe test of the ability of L to identify small inconsistencies, an artifact was produced by converting a single soft-tissue pixel to bone value as shown in figure 7.

IV. Evaluation Results

A. Detection/Correction Algorithm

Figure 8 shows the recovered attenuation map after each of nine iterations of the detection/ correction algorithm, and figure 9 shows the corresponding activity images. For display purposes, to compensate for the differing emission-image frequency content at each iteration, post-algorithm filtering was applied to the activity images to approximately reproduce the texture of the image shown in figure 9, top row, right.

Figure 8 shows the artifact fading out of the attenuation image as the algorithm progresses. Some degradation to the remainder of the dynamic region can be seen including reduction of values of some true-bone (R2) pixel values, but also relatively large μ values in scattered R2 pixels.

Quantitatively, after 9 iterations of the reconstruction/ recovery algorithm, the value of ME_R ($RMSE_R$) of the initially artifactual region, R1, improved from 99% to 8.7% (99% to 16%). In the initially correct part, R2, of the dynamic region, ME_R ($RMSE_R$) deteriorated only slightly from 0% to −7.2% (0% to 8.3%). The per pixel $RMSE_{Rp}$ values were found to improve from 99% to 31% in the initially artifactual region R1 with a deterioration from 0% to 30% in the initially correct region (R2). The emission images in figure 9 show that the algorithm works to the point that it is difficult to distinguish the artifact-free (ideal) image (top row, left) from the recovered image (bottom row, iteration 9). In the emission images, little or no residual (R1) or induced (R2) artifact can be observed, with the effects on the emission image of artifacts in the final attenuation map being dwarfed by noise in the emission data.

The results of the ROC study for the task of detecting anomalous pixel-values are shown in Figure 10. The area under the ROC curve is $AUC = 0.90$.

B. Likelihood Information Content

1) Bone-like Inconsistencies in Soft Tissue—Figure 11 shows results of the study in which 2 cm^2 (13-pixel) bone-valued attenuation artifacts were inserted into the chest and shoulder attenuation maps. Accuracy was not strongly dependent on the particular slice under study. Excellent accuracy is seen for simulated sinogram count levels greater than 10000. (The noise level at 10000 simulated counts is illustrated in figures 4d and 4h.) At 50000 simulated counts an accuracy of 95% is observed in the chest and 90% in the shoulder. Even at the very noisy simulated count level of 1000, accuracies significantly greater than chance (50%) are observed.

Figure 12 shows accuracy results when the task was to distinguish a larger artifact from a smaller artifact. In this study the loglikelihood classification accuracy at a simulated sinogram count level of 50000 was found to be 98% for the chest slice and 87% for the shoulder slice. In this case there are differences between chest and shoulder accuracy, with

shoulder accuracy being less over most of the simulated count region. Again, even at the level of 1000 simulated sinogram counts, accuracy is significantly better than chance.

2) Soft Tissue-like Inconsistencies in Bone—Figure 13 shows accuracy results when the task was to distinguish an artifact in which a small region of bone has been misclassified as soft tissue. Accuracies of 96% and 98% were observed in the chest and shoulder slices respectively at a simulated sinogram count level of 50000. Accuracy drops to chance levels at 1000 simulated sinogram counts in the shoulder slice.

3) Intermediate-Valued Artifacts in Soft Tissue—Accuracy as a function of simulated sinogram count level for a 13-pixel artifact in soft-tissue with a μ-value intermediate between bone and soft-tissue is illustrated in figure 14. Particularly at low simulated count levels, accuracy falls below the values found in the case of a similarly shaped artifact but with a higher μ-value (figure 11).

4) Single Pixel—The classification accuracy of L for the case in which the artifact is a single pixel with value of bone in place of soft tissue is illustrated in figure 15. As expected, accuracy at all simulated sinogram count levels for the single-pixel artifact falls below the corresponding values for the case of a larger artifact of similar nature (figure 11). At a simulated sinogram count level of 50000, accuracies of 71% in the chest slice and 69% in the shoulder slice were found. Accuracies in the chest and shoulder were similar over the domain of count levels studied. Accuracy is also observed to be an approximately linear function of $\ln(C)$ for $10^3 < C < 10^7$, where C is the simulated sinogram count level.

V. Discussion

A variety of transformation algorithms have been proposed for converting CT-values to 511-keV μ-values. While the results of commonly used methods are generally good for most clinical applications, they depend on assumptions regarding the atomic composition of various material within the scanned patient. The precise nature of the incorporated assumptions leads to various biases in the final image [37]. Of concern is that anomalous material can cause serious inaccuracies in the attenuation image and in the final PET emission image. Conversion algorithms can be designed that reduce the effect of certain types of artifacts. For example, the effect of localized contrast as investigated here can be reduced through the use of algorithms that cap μ-values at soft tissue values (e.g. [38][39]. However, such a solution increases bias - in this example, by forcing bone regions to have soft tissue-like μ-values. Our results suggest that a more complete use of the available data can identify anomalous material without the cost of increased image bias.

This work has some similarities to previous work investigating the problem of joint reconstruction of full attenuation and emission images from emission data alone. However, such methods are complicated by the underdetermined nature of the problem, Researchers have handled this by various methods. For example, Nuyts et al. [19], use a μ-value probability distribution prior that drives their algorithm towards assigning predefined μ-values typical of assumed material classes, e.g. soft tissue, air, or lung. Even so, based on a study using a digital thorax phantom containing lung, soft tissue, and air (but not bone), the authors concluded, "... extension [of the algorithm] to nonuniform attenuation in the lungs may be possible in SPECT [Single Photon Emission Computed Tomography], but will be difficult in PET." An advantage of the algorithm presented in the current work is that it is designed specifically for the task of identifying and correcting attenuation artifacts; it operates using a given and mostly high quality attenuation map as input and does not modify μ-values in the static region, comprising most of the image including lungs and soft tissue.

Thus the current algorithm bypasses some of the difficult issues in performing a joint reconstruction without attenuation data.

A limitation of this work is that the presented algorithm contains parameters that were not rigorously optimized, but which should be in a more comprehensive study. Parameters include the number subsets and iterations used in OSEM (type 2 procedure of Fig. 2) as well as the number of iterations of the full (type-1 + type-2 procedure) algorithm, As implemented here, the ICD algorithm (type 1 procedure) contains adjustable penalty parameters for attenuation (the exponent q of Eq. 9 and the penalty strength β of Eq. 2). Although not used here, a similar penalty could be applied during the emission update.

Using the algorithm in a relatively high-noise scenario, artifacts were nearly eliminated in the transmission and emission images. However, the algorithm also degraded some regions of true bone (R2) in the attenuation image, including the introduction of high μ values in isolated pixels. This may be related to the to the nature of the type-1 procedure in which image pixels are updated individually. We note that the purpose of the attenuation penalty is to discourage such behavior, however, too large a penalty inhibits the ability of the algorithm to detect or eliminate actual contrast artifacts.

Nevertheless, the algorithm is potentially useful for tasks of detection (as shown by the ROC results) and correction (as shown by Figures 8 and 9 and by the performance figures of merit) of anomalous-material induced attenuation artifacts.

There are several modes of operation in which a detection/correction algorithm similar to the one presented here could be used in the clinic. In one mode, clinical reads are performed directly on the algorithm output (i.e., the recovered emission image). The FOMs of equation 10, calculated in the Results section suggest that this is a viable possibility.

An alternate mode is to use the algorithm to detect and localize suspected artifacts. A map of the location of detected artifacts would be prepared and presented to the radiologist for follow up. Such a map could be constructed, for example, by flagging areas of the dynamic region in which μ values showed large decreases compared to their initial values. The ROC results indicate that this also is a reasonable approach.

A key element in the design of algorithms for detecting and correcting errors in an attenuation map is the ability of an objective function to distinguish between more and less artifactual attenuation images in the presence of statistical noise. Thus the second focus of this work (Section III-C) gauged the ability of the loglikelihood for this task, independent of any particular estimation procedure. The results show that the loglikelihood is able to perform this task for a variety of situations at reasonable simulated count levels (see Figures 11–15 and also figure 4 to relate simulated count levels to image quality). Classification accuracies were typically 85% or better for 2 cm^2 (13-pixel) regions and simulated sinogram counts of at least 10,000, which, based on Fig. 4 corresponds to a relatively high-noise acquisition.

In all studies, results have been presented as a function of simulated sinogram count level. The statistical effects of scatter and random corrections have not been directly addressed. Thus the quoted count levels cannot be compared directly to clinical count rates for most imaging situations, but should be used in a relative manner with Fig. 4 setting an overall scale. Additionally, certain imaging issues including the effects of imperfect PET resolution and possible misregistration between PET and CT were not considered. The use of simulated data in which the ground truth is known allowed a detailed investigation of objective function performance and of the performance of a complete algorithm. However its clinical utility requires more extensive studies, including those with patient data.

The focus of this work was on the detection of contrast media. Similar procedures could be used to address similar problems that arise due to other types of anomalous material that improperly scales from CT units to 511 keV μ values such as dental or surgical implants.

VI. Conclusion

A likelihood-based algorithm for the correction of CT contrast media induced artifacts in PET attenuation correction images in the PET/CT modality has been developed and tested. The algorithm exploits the fact that contrast artifacts manifest as high values of μ in an otherwise high quality attenuation image. Additionally the performance of the loglikelihood as an objective-function component of a detection/correction algorithm, independent of any particular algorithm was mapped out for several imaging scenarios as a function of statistical noise. Both the full algorithm and the loglikelihood performed well in simulation studies. Additional studies including those with patient data are required to fully understand their capabilities.

Acknowledgments

The authors would like to thank Dr. Todd Blodgett for his insightful comments and for providing Fig. 1. This work was supported by NIH grants R21 EB002622, P30 CA47904, and R21 CA156390.

References

1. Berger, M.; Hubbell, J.; Seltzer, S.; Chang, J.; Coursey, J.; Sukumar, R.; Zucker, D. XCOM: Photon cross section database (version 1.3). National Institute of Standards and Technology; Gaithersburg, MD: 2006 Jan 31. Available: http://physics.nist.gov/xcomvol. online, 2005
2. Beyer T, Townsend DW, Brun T, Kinahan PE, Charron M, Roddy R, Jerin J, Young J, Byars L, Nutt R. A combined PET/CT scanner for clinical oncology. J Nucl Med. 2000; 41:1369–1379. [PubMed: 10945530]
3. Kinahan PE, Townsend DW, Beyer T, Sashin D. Attenuation correction for a combined 3D PET/CT scanner. Med Phys. 1998; 25:2046–2053. [PubMed: 9800714]
4. Burger C, Goerres G, Schoenes S, Buck A, Lonn AHR, von Schulthess GK. PET attenuation coefficients from CT images: experimental evaluation of the transformation of CT into PET 511-kev attenuation coefficients. Eur J Nucl Med Mol Imaging. 2002; 29:922–927. [PubMed: 12111133]
5. Bai CY, Shao L, Da Silva AJ, Zhao Z. A generalized model for the conversion from ct numbers to linear attenuation coefficients. IEEE Transactions On Nuclear Science. 2003; 50:1510–1515.
6. Kinahan PE, Hasegawa BH, Beyer T. X-ray-based attenuation correction for positron emission tomography/computed tomography scanners. Seminars In Nuclear Medicine. 2003; 33:166–179. [PubMed: 12931319]
7. LACROIX, K.; TSUI, B.; HASEGAWA, B.; BROWN, J. INVESTIGATION OF THE USE OF X-RAY CT IMAGES FOR ATTENUATION COMPENSATION IN SPECT. IEEE TRANSACTIONS ON NUCLEAR SCIENCE; Nuclear Science Symposium and Medical Imaging Conference (NSS-MIC 93); SAN FRANCISCO, CA. OCT 30-NOV 06, 1993; Dec. 1994 p. 2793-2799.
8. Blankespoor SC, Wu X, Kalki K, Brown JK, Tang HR, Cann CE, Hasegawa BH. Attenuation correction of spect using x-ray ct on an emission-transmission ct system: Myocardial perfusion assessment. IEEE Transactions On Nuclear Science. 1996; 43:2263–2274.
9. Antoch G, Freudenberg LS, Egelhof T, Stattaus J, Jentzen W, Debatin JF, Bockisch A. Focal tracer uptake: A potential artifact in contrast-enhanced dual-modality PET/CT scans. J Nucl Med. 2002; 43:1339–1342. [PubMed: 12368372]
10. Censor Y, Gustafson DE, Lent A, Tuy H. A new approach to the emission computerized tomography problem: Simultaneous calculation of attenuation and activity coefficients. IEEE Trans Nucl Sci. 1978; 26:2775–2779.

11. Natterer F. Computerized tomography with unknown sources. SIAM J Appl Math. 1983; 43:1201–1212.
12. Manglos, HS.; Young, TM. Constrained intraSPECT reconstruction from SPECT projections. ser. Nuclear Science Symposium and Medical Imaging Conference; IEEE. Nov. 1993; p. 1603-1609.
13. Bronnikov AV. Approximate reconstruction of attenuation map in SPECT imaging. IEEE Trans Nucl Sci. 1995; 42:1483–1488.
14. Welch A, Clack R, Natterer F, Gullberg GT. Toward accurate attenuation correction in SPECT without transmission measurements. IEEE Trans Med Imaging. 1997; 16:532–541. [PubMed: 9368109]
15. Welch A, Campbell C, Clackdoyle R, Natterer F, Hudson M, Bromiley A, Mikecz P, Chillcot F, Dodd M, Hopwood P, Craib S, Gullberg GT, Sharp P. Attenuation correction in PET using consistency information. IEEE Trans Nucl Sci. 1998; 45:3134–3141.
16. Bronnikov AV. Numerical solution of the identification problem for the attenuated radon transform. Inverse Probl. 1999; 15:1315–1324.
17. Dicken V. A new approach towards simultaneous activity and attenuation reconstruction in emission tomography. Inverse Probl. 1999; 15:931–960.
18. Laymon CM, Turkington TG. Calculation of attenuation factors from combined singles and coincidence emission projections. IEEE Trans Med Imaging. 1999; 18:1194–1200. [PubMed: 10695532]
19. Nuyts J, Dupont P, Stroobants S, Benninck R, Mortelmans L, Suetens P. Simultaneous maximum a posteriori reconstruction of attenuation and activity distributions from emission sinograms. IEEE Trans Med Imaging. 1999; 18:393–403. [PubMed: 10416801]
20. Bronnikov AV. Reconstruction of attenuation map using discrete consistency conditions. IEEE Trans Med Imaging. 2000; 19:451–462. [PubMed: 11021688]
21. Krol A, Bowsher JE, Manglos SH, Feiglin DH, Tornai MP, Thomas ED. An EM algorithm for estimating SPECT emission and transmission parameters from emission data only. IEEE Trans Med Imaging. 2001; 20:218–232. [PubMed: 11341711]
22. Gourion D, Noll D, Gantet P, Celler A, Esquerre JP. Attenuation correction using SPECT emission data only. IEEE Trans Nucl Sci. 2002; 49:2172–2179.
23. Landmann M, Reske SN, Glatting G. Simultaneous iterative reconstruction of emission and attenuation images in positron emission tomography from emission data only. Med Phys. 2002; 29:1962–1967. [PubMed: 12349915]
24. Crepaldi F, De Pierro AR. Activity and attenuation reconstruction for positron emission tomography using emission data only via maximum likelihood and iterative data refinement. IEEE TRANSACTIONS ON NUCLEAR SCIENCE. Feb; 2007 54(1 Part 1):100–106.
25. Shepp LA, Vardi Y. Maximum likelihood reconstruction for emission tomography. IEEE Trans Med Imaging. 1982; 2:113–122. [PubMed: 18238264]
26. Mumcuoglu E, Leahy R, Cherry S, Zhou Z. Fast gradient-based methods for Bayesian reconstruction of transmission and emission PET images. IEEE Trans Med Imag. 1994; 13(4): 687–701.
27. Zheng J, Saquib SS, Sauer K, Bouman CA. Parallelizable Bayesian tomography algorithms with rapid, guaranteed convergence. IEEE Trans Image Process. 2000; 9:1745–1759. [PubMed: 18262913]
28. Nuyts J, Fessler JA. A penalized-likelihood image reconstruction method for emission tomography, compared to postsmoothed maximum-likelihood with matched spatial resolution. IEEE Transactions On Medical Imaging. 2003; 22:1042–1052. [PubMed: 12956260]
29. Hsiao IT, Rangarajan A, Khurd P, Gindi G. An accelerated convergent ordered subsets algorithm for emission tomography. Physics in Medicine and Biology. 2004; 49(11):2145–2156. [PubMed: 15248569]
30. Erdogan H, Fessler JA. Monotonic algorithms for transmission tomography. IEEE Trans Med Imaging. 1999; 18:801–814. [PubMed: 10571385]
31. Erdogan H, Fessler JA. Ordered subsets algorithms for transmission tomography. Phys Med Biol. 1999; 44:2835–2851. [PubMed: 10588288]

32. Bouman CA, Sauer K. A generalized Gaussian image model for edge-preserving MAP estimation. IEEE Trans Image Process. 1993; 2:296–310. [PubMed: 18296219]
33. Bouman CA, Sauer K. A unified approach to statistical tomography using coordinate descent optimization. IEEE Trans Image Process. 1996; 5:480–492. [PubMed: 18285133]
34. Hudson HM, Larkin RS. Accelerated image-reconstruction using ordered subsets of projection data. IEEE Trans Med Imaging. 1994; 13:601–609. [PubMed: 18218538]
35. Zubal IG, Harrell CR, Smith EO, Rattner Z, Gindi G, Hoffer PB. Computerized 3-dimensional segmented human anatomy. Med Phys. 1994; 21:299–302. [PubMed: 8177164]
36. Lewellen, TK.; Harrison, RL.; Vannoy, S. The SimSET program. In: Ljungberg, M.; Strand, SE.; King, MA., editors. Monte Carlo Calculations in Nuclear Medicine: Applications in Diagnostic Imaging. Philadelphia, PA: Inst. Phys; 1998. p. 77-92.
37. Ay MR, Shirmohammad M, Sarkar S, Rahmim A, Zaidi H. Comparative Assessment of Energy-Mapping Approaches in CT-Based Attenuation Correction for PET. MOLECULAR IMAGING AND BIOLOGY. Feb; 2011 13(1):187–198. [PubMed: 20387123]
38. Nuyts, J.; Stroobants, S. Reduction of attenuation correction artifacts in pet-ct. Nuclear Science Symposium Conference Record, 2005 IEEE; oct. 2005; p. 5
39. Lemmens C, Nuyts J, Dirix S, Stroobants S. Reduction of the influence of intravenous contrast in PET/CT by using a threshold conversion method. IEEE TRANSACTIONS ON NUCLEAR SCIENCE. Oct; 2007 54(5 Part 1):1687–1695.

Biographies

Charles Laymon is a Research Assistant Professor of Radiology and Bioengineering at the University of Pittsburgh. His research interests include PET hardware development and PET, MR, and CT image processing and methodology for cancer therapy evaluation.

James Bowsher is Assistant Professor of Radiation Oncology at Duke University Medical Center. His research interests include instrumentation and image reconstruction for nuclear medicine and molecular and functional imaging for radiation therapy.

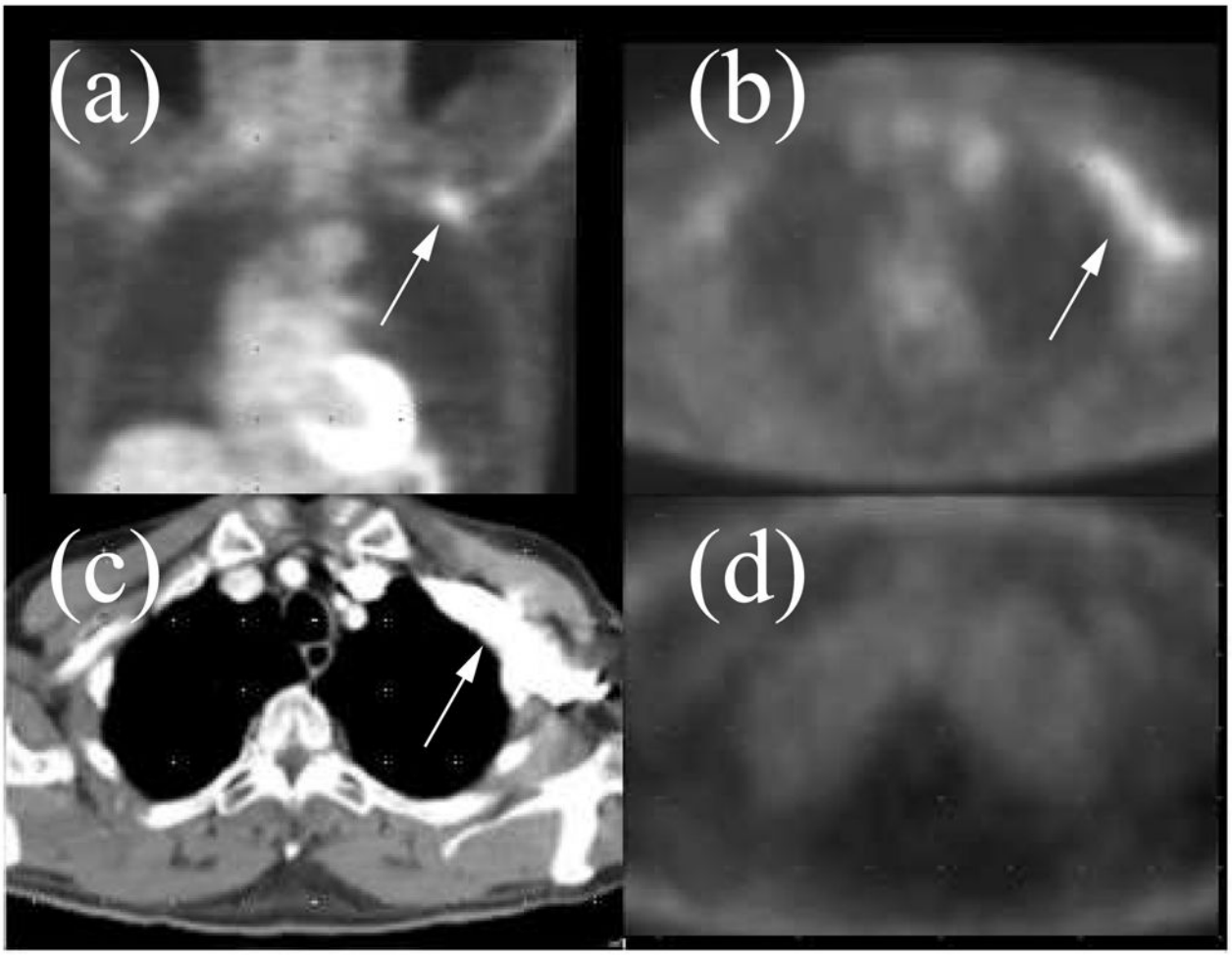

Fig. 1.
Clinical PET/CT with CT contrast agent. The top row shows coronal (a) and transaxial (b) attenuation-corrected PET images. The arrows indicate a region that is believed to be an artifact from contrast agent. This conclusion is based upon an examination of the CT image showing probable contrast enhancement indicated by the arrow (c) and the uncorrected PET image in which abnormal tracer uptake is not evident.

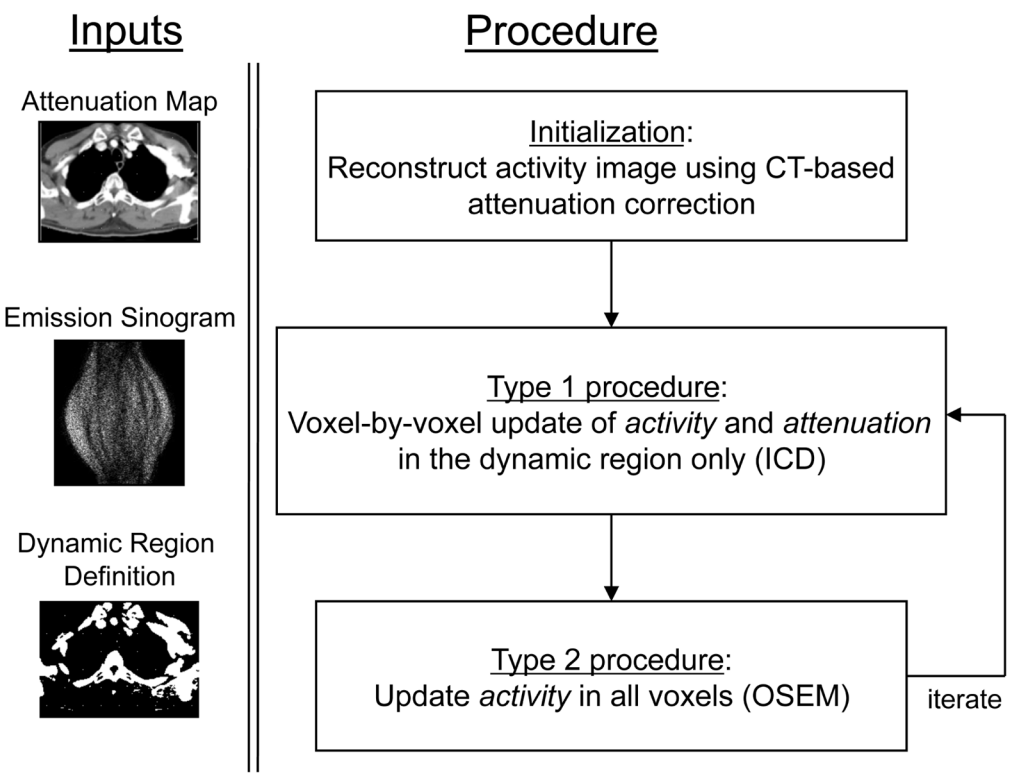

Fig. 2.

Schematic of the operation of the recovery algorithm. The PET data is first reconstructed using the CT-based attenuation correction. An iterative method consisting of two procedures is than applied. In the type 1 procedure, pixel-wise updates, within the dynamic region, of both attenuation and emission are performed using ICD[33]. In the type 2 procedure all emission values throughout the image are updated using OSEM[34].

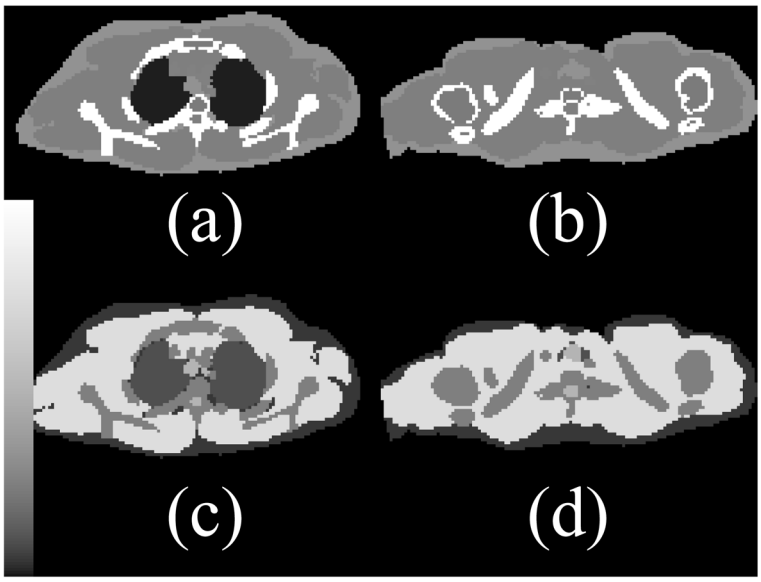

Fig. 3.
The true attenuation distribution for the chest (a) and shoulder (b) and the corresponding true activity distribution for the chest (c) and shoulder (d).

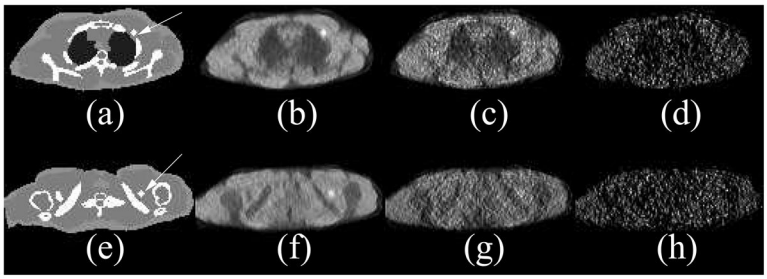

Fig. 4.

Attenuation image with a 13-pixel artifact marked by arrow for the chest (a) and shoulder (e). The artifact was produced by assigning bone-valued attenuation coefficients to soft tissue. Sample emission reconstructions using the artifactual attenuation are also shown for varying sinogram count densities: 10^6 (b), 10^5 (c), and 10^4 (d) for the chest slice. Parts (f–h) show similar reconstructions for the shoulder slice. In each case, OSEM reconstructions were performed using 4 iterations of 9 subsets with no post reconstruction filtering.

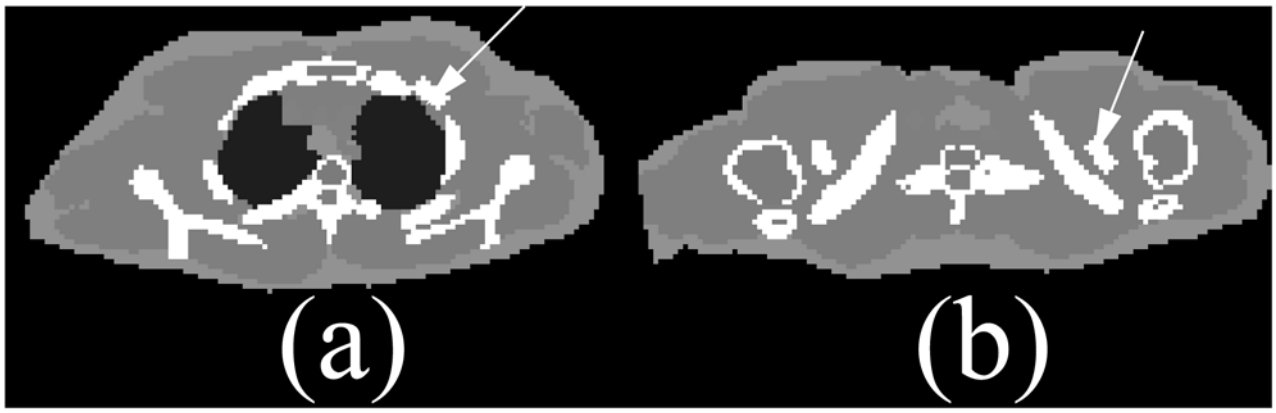

Fig. 5.
Attenuation images similar to those of figure 4 containing two adjacent 13-pixel artifactual regions marked by an arrow for the chest (a) and the shoulder (b).

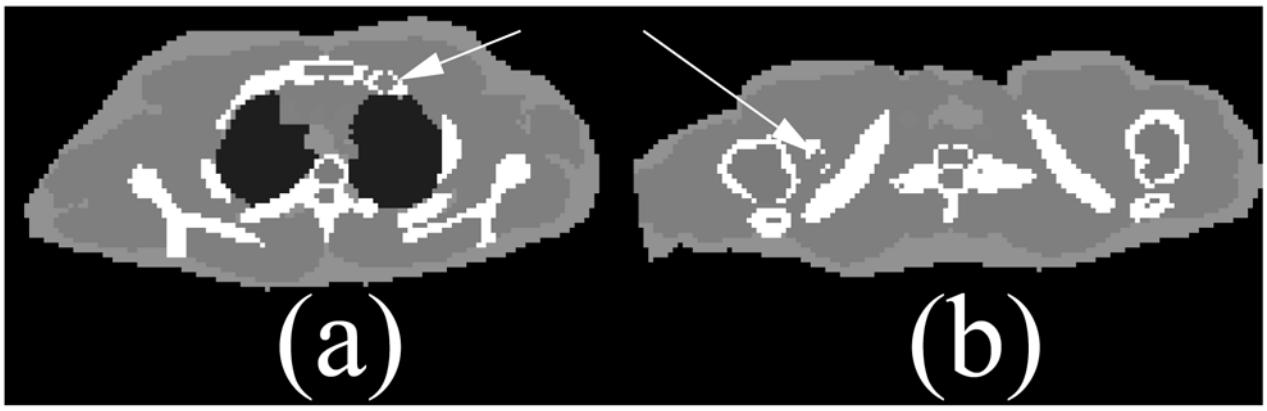

Fig. 6.
Attenuation artifacts marked by arrow for the chest (a) and the shoulder (b) have the μ-value for soft tissue in place of bone.

Fig. 7.
Attenuation images with single-pixel bone-valued artifacts in place of soft tissue are marked by arrows in the chest (a) and shoulder (b).

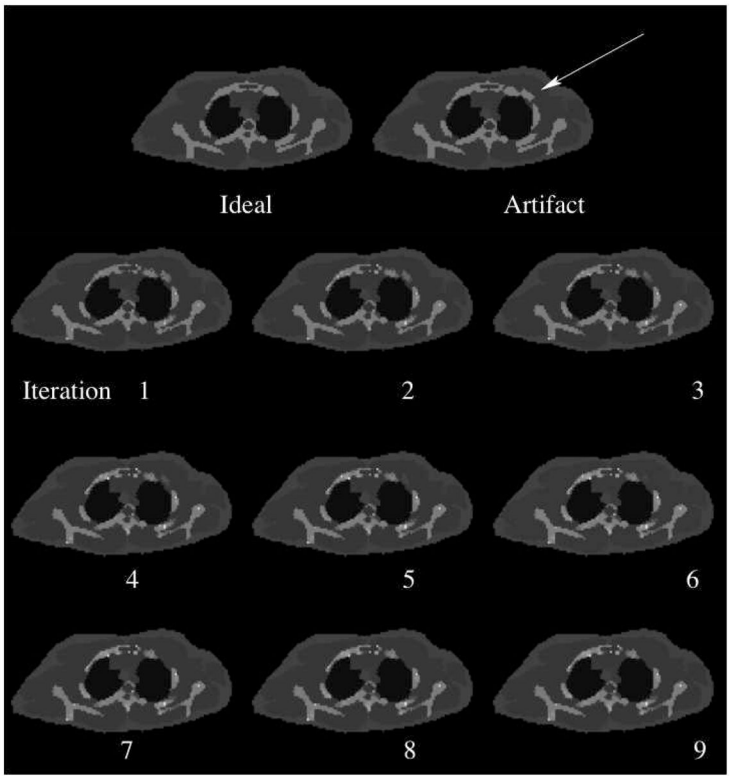

Fig. 8.

Algorithm results for 100000 simulated sinogram counts: attenuation images. Top row shows the true attenuation map (left) and an attenuation map with an artifact marked by an arrow (right). The subsequent rows show the recovered attenuation map after each iteration of the algorithm described in the text.

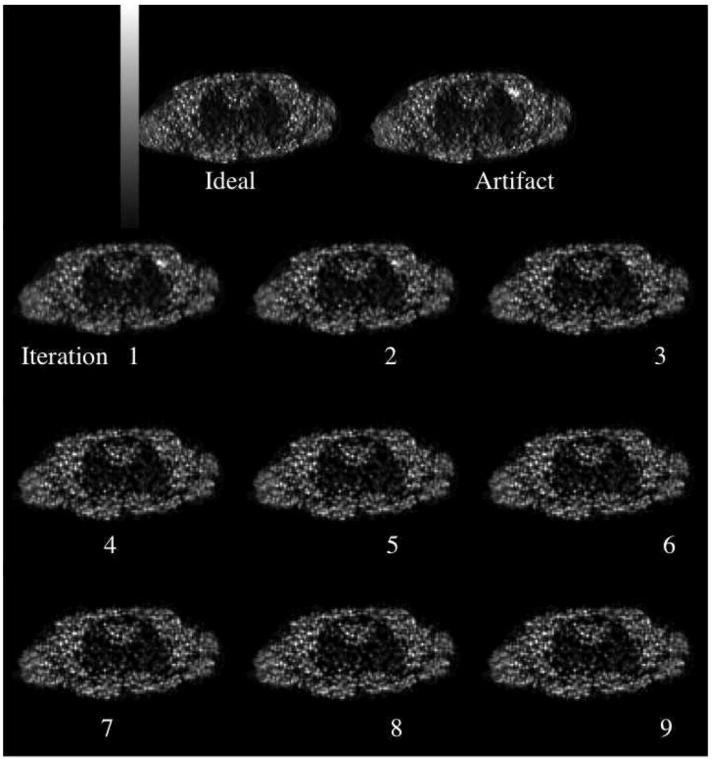

Fig. 9.
Algorithm results for 100000 simulated sinogram counts: activity images. The activity images in this figure correspond to the attenuation images in figure 9. Top row shows the activity images obtained with the true attenuation map (left) and the artifactual attenuation map (right). These images were reconstructed using OSEM with 9 subsets and 4 iterations. The subsequent rows show the emission image after each iteration of the algorithm described in the text.

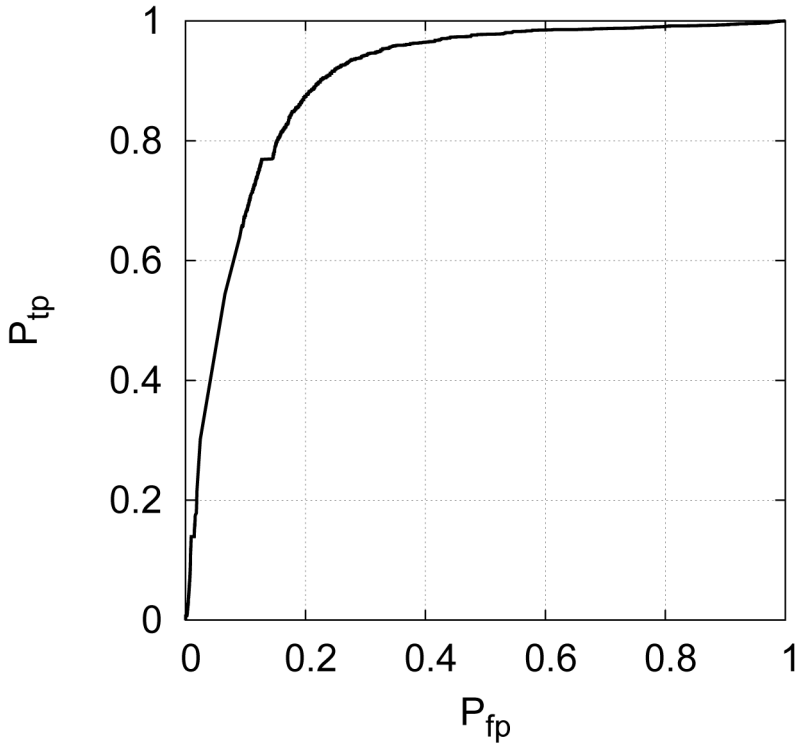

Fig. 10.
ROC curve for the task of detection of bone-like artifacts in the 100000 simulated count sinograms. P_{tp} and P_{fp} are true-positive and false-positive rates for artifact detection.

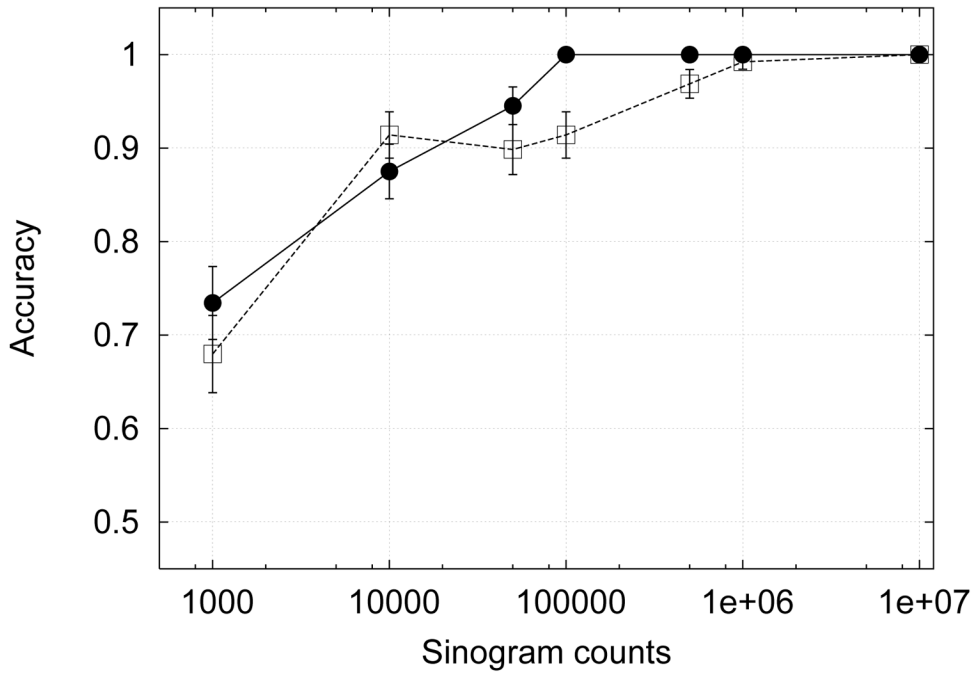

Fig. 11.

2.1-cm^2 (13-pixel) bone-valued artifact in soft tissue in the chest (solid circles) and shoulder (open squares) - Plots of loglikelihood classification accuracy as a function of simulated sinogram count. The task was to identify the artifact-free attenuation image. Connecting lines are shown to guide the eye.

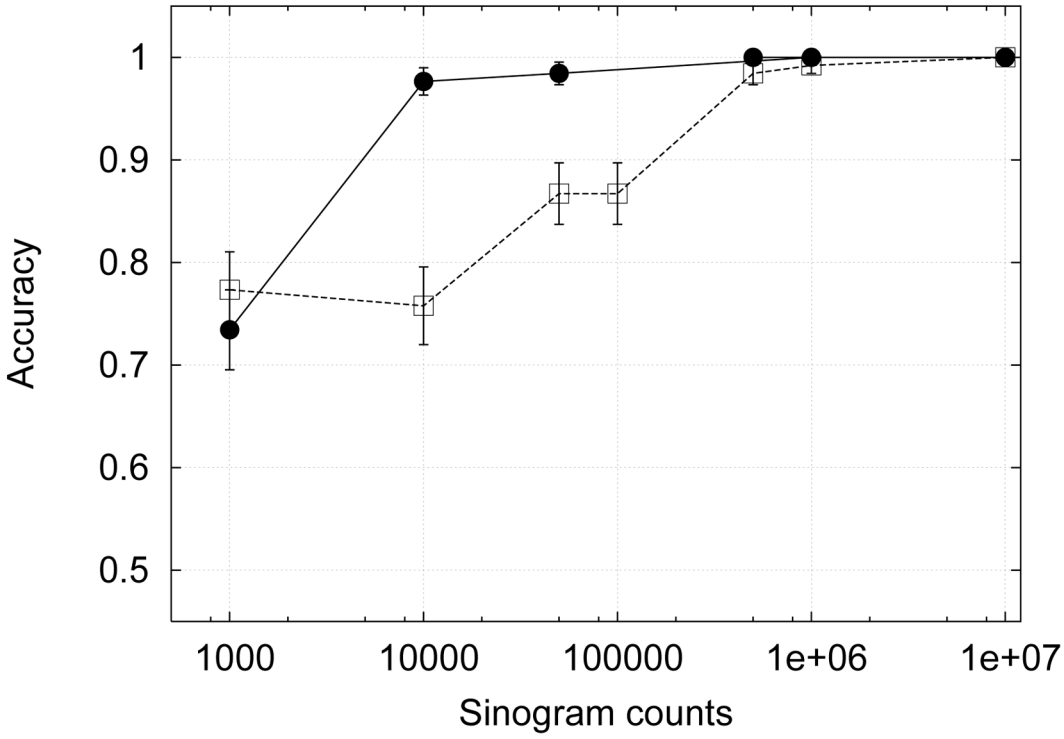

Fig. 12.

2 2.1-cm^2 (13-pixel) artifacts in the chest (solid circles) and shoulder (open squares) - Plots of loglikelihood classification accuracy as a function of simulated sinogram count level. The task was to identify the image with one 13-pixel artifact compared to the image with two artifacts.

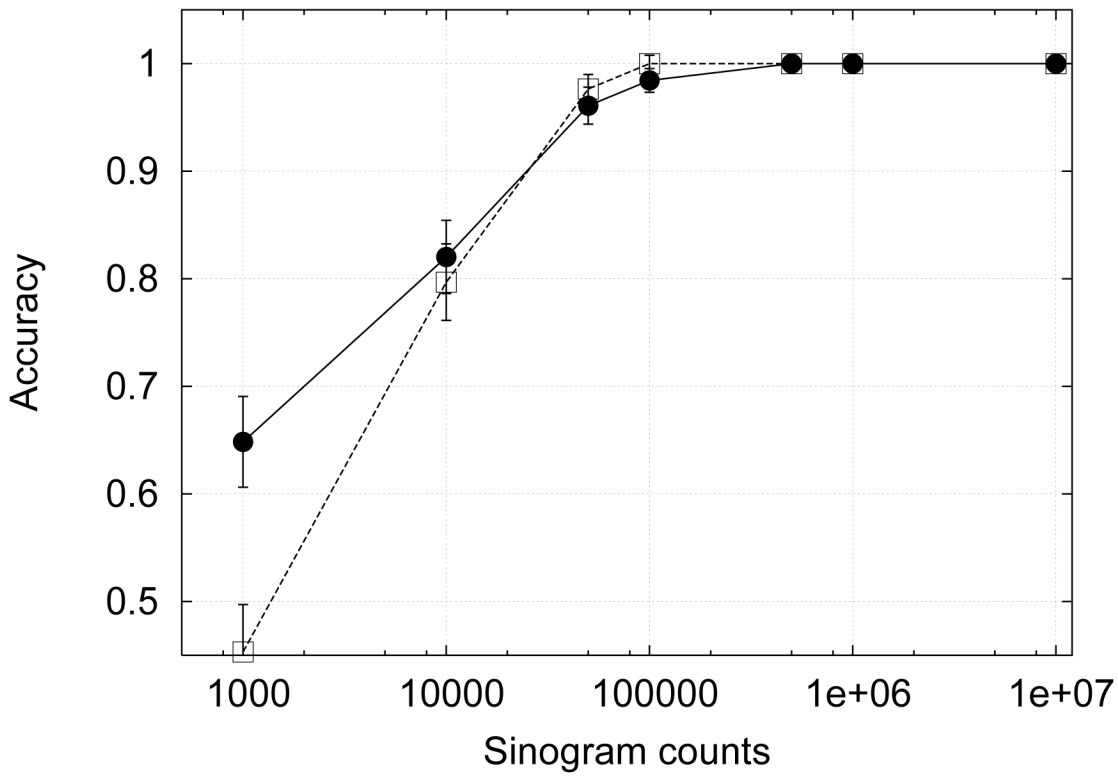

Fig. 13.
2.1-cm^2 (13-pixel) soft-tissue-valued artifact in bone in the chest (solid circles) and shoulder (open squares)- Plots of loglikelihood classification accuracy as a function of simulated sinogram count level.

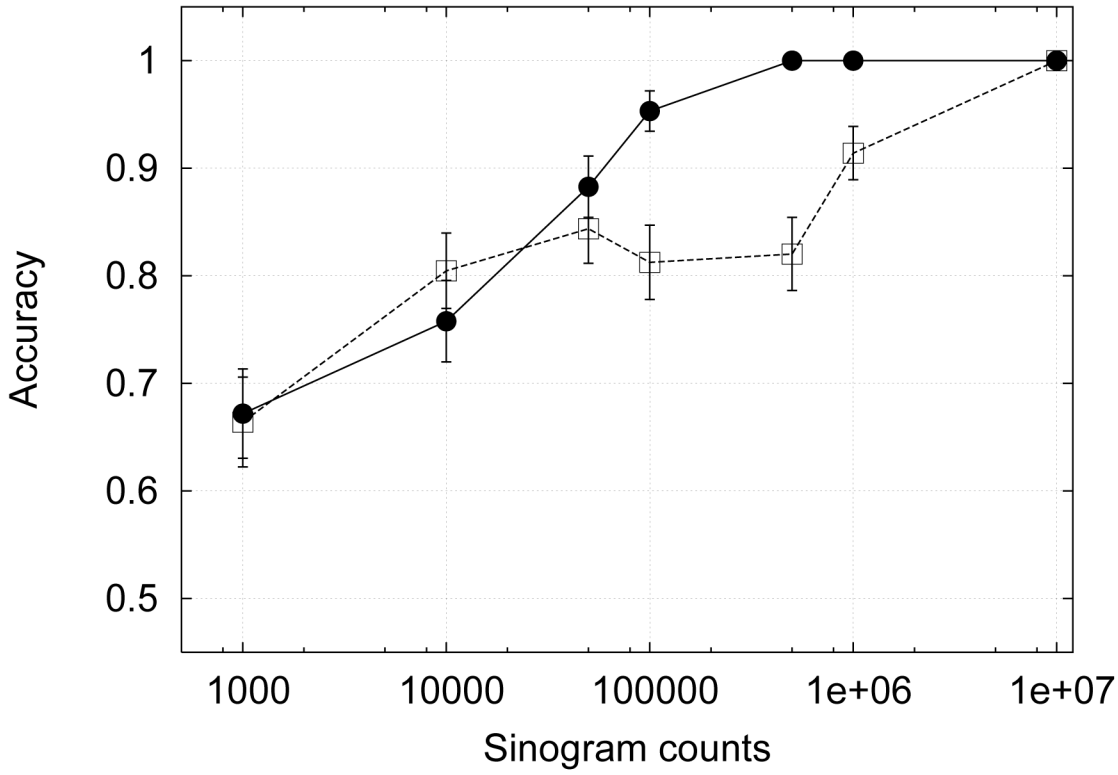

Fig. 14.
Soft-tissue artifact with a μ-value intermediate between soft tissue and bone in the chest (solid circles) and shoulder (open squares) - Plots of accuracy as a function of simulated sinogram count level

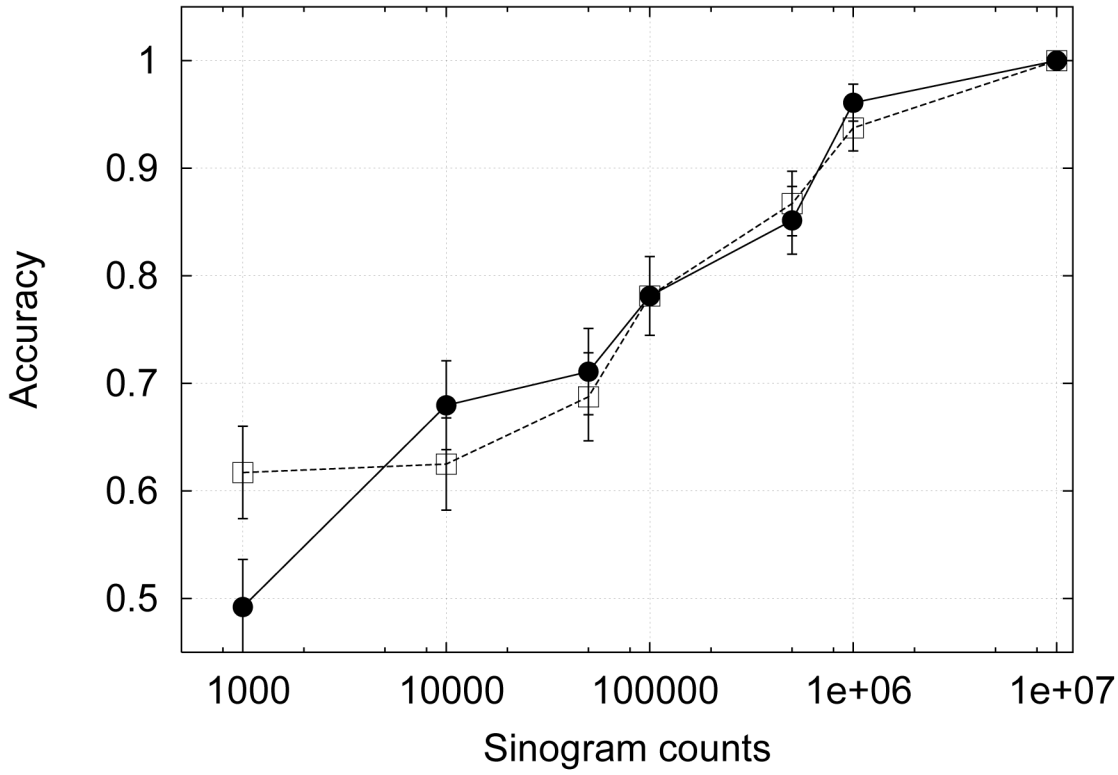

Fig. 15.
0.16-cm^2 (1-pixel) bone valued artifact in place of soft tissue in the chest (solid circles) and shoulder (open squares) - Plots of accuracy as a function of simulated sinogram count level.